PHOTONICS Research

Ge-on-Si modulators operating at mid-infrared wavelengths up to 8 μm

Tiantian Li,[1,2] Milos Nedeljkovic,[1] Nannicha Hattasan,[1] Wei Cao,[1] Zhibo Qu,[1] Callum G. Littlejohns,[1,3] Jordi Soler Penades,[1] Lorenzo Mastronardi,[1] Vinita Mittal,[1] Daniel Benedikovic,[4] David J. Thomson,[1] Frederic Y. Gardes,[1] Hequan Wu,[2] Zhiping Zhou,[2] and Goran Z. Mashanovich[1,*]

[1]Optoelectronics Research Centre, University of Southampton, Southampton SO17 1BJ, UK
[2]State Key Laboratory of Advanced Optical Communication Systems and Networks, School of Electronics Engineering and Computer Science, Peking University, Beijing 100871, China
[3]Silicon Technologies Centre of Excellence, Nanyang Technological University, Singapore 639798, Singapore
[4]Centre de Nanosciences et de Nanotechnologies, CNRS, Univ. Paris-Sud, Université Paris-Saclay, C2N—Palaiseau, 91120 Palaiseau, France
*Corresponding author: g.mashanovich@soton.ac.uk

Received 19 December 2018; revised 8 May 2019; accepted 27 May 2019; posted 28 May 2019 (Doc. ID 353165); published 12 July 2019

We report mid-infrared Ge-on-Si waveguide-based PIN diode modulators operating at wavelengths of 3.8 and 8 μm. Fabricated 1-mm-long electro-absorption devices exhibit a modulation depth of >35 dB with a 7 V forward bias at 3.8 μm, and a similar 1-mm-long Mach–Zehnder modulator has a $V_\pi \cdot L$ of 0.47 V · cm. Driven by a 2.5 V_{pp} RF signal, 60 MHz on-off keying modulation was demonstrated. Electro-absorption modulation at 8 μm was demonstrated preliminarily, with the device performance limited by large contact separation and high contact resistance.

Published by Chinese Laser Press under the terms of the Creative Commons Attribution 4.0 License. Further distribution of this work must maintain attribution to the author(s) and the published article's title, journal citation, and DOI.
https://doi.org/10.1364/PRJ.7.000828

1. INTRODUCTION

Silicon photonics has attracted great research interest over the last decade for its prospects in the creation of integrated devices for near-infrared (NIR) wavelengths, especially for use in optical interconnects and communications systems [1–6]. The motivation for investigating wavelengths further into the mid-infrared (MIR), defined here as wavelengths in the range 2–15 μm, comes from the applications that are possible for photonics in this range. Integration of MIR devices could be used to create "lab-on-a-chip" type sensors, which could be used for environmental pollution monitoring, toxic chemical detection for homeland security, and noninvasive methods of early disease diagnosis, to name a few. In addition, the MIR range also contains two atmospheric transmission windows (3–5 μm and 8–12 μm) and thus offers a new spectrum for free-space light transmission [7].

Silicon is now widely used for NIR photonics. Silicon-on-insulator (SOI) technology has been used as an established photonic platform for the NIR, with several multi-project wafer services that offer access to sophisticated but affordable fabrication processes. However, silicon dioxide (SiO_2) has high material absorption in the 2.6–2.9 μm range and beyond 3.6 μm [8], which limits the use of SOI platforms. Many new platforms with extended transparency ranges have been proposed for MIR photonics. This includes silicon-on-sapphire [9], silicon-on-nitride [10], germanium-on-insulator [11], SiGe graded index-on-silicon (SiGe-on-Si) [12–14], germanium-on-silicon (Ge-on-Si) [15,16], germanium-on-nitride [17], and chalcogenide glasses [18]. In germanium-rich graded silicon–germanium waveguides, a low loss of 2–3 dB/cm [13] and supercontinuum generation [14] have both been demonstrated up to the 8.5 μm wavelength. For MIR light transmission, Ge is recognized as an ideal material since it exhibits high transparency over nearly the entire MIR range (2–16 μm) [19]. Based on the transparency windows of bulk Ge and Si, the Ge-on-Si platform is expected to provide a wide MIR wavelength range together with facile processing. Low-loss Ge-on-Si waveguide transmission has been shown in Refs. [16,20–22], with Ref. [21] demonstrating low losses up to 11.25 μm. Moreover, other Ge-on-Si devices like planar concave gratings [23], multimode interferometers [20], arrayed waveguide gratings [24], as well as surface grating couplers [25] have been reported.

However, waveguide-integrated modulators based on the Ge-on-Si platform have been little explored so far. The only previous demonstration is a thermo-optic modulator [26] operating at 5 μm. On-chip modulators might find a number of

uses for MIR wavelengths. (i) Free-space communication systems exploiting the MIR transmission windows would require high-speed modulators. (ii) Frequently, choppers are used in combination with lock-in amplifiers to increase the signal-to-noise ratio (SNR) of MIR measurement systems [27,28]. The chopper in such a system could be replaced by an on-chip modulator to make on-chip MIR systems more sensitive. (iii) 1 × 2 switches would be useful for on-chip sensors, for example, for switching light between a waveguide that is exposed to an analyte and a reference waveguide, to remove external sources of noise. (iv) On-chip beam steering systems similar to those currently being explored in Si photonics in the NIR for LIDAR may be useful for a range of MIR applications, and they would require waveguide-integrated phase shifters.

Bulk Ge has a thermo-optic coefficient 3 times larger than that in Si. However, Ge-on-Si thermo-optic modulators, as demonstrated in Ref. [26], exhibited comparatively low efficiency, since 700 mW power level was required for a 2π phase shift. The high thermal conductivity of the Si substrate was only improved by using Ge-on-SOI wafers [26] or creating suspended Ge waveguide membranes [29], both of which improved the thermal isolation of the waveguide. Aside from the power efficiency issue, the speed of the thermo-optic effect intrinsically limits the modulation frequency to approximately 10–100 kHz. In order to improve both the efficiency and the bandwidth, it is necessary to explore other electro-optic effects in Ge.

Due to the centrosymmetric crystal structure of Ge, the Pockels effect is weak, while the Kerr effect is also weak in Ge, and the Franz–Keldysh effect is negligible for wavelengths longer than ~1.6 μm. The free-carrier plasma effect in Ge has been numerically calculated from a combination of theory and experimental data in Ref. [30]. It was predicted that Ge modulators exploiting free-carrier absorption at a wavelength of 3.8 μm should be almost 4 times more effective than in Si [30]. An electro-absorption modulator on a germanium-on-insulator (GeOI) platform was reported in 2016 [11]. However, high SiO_2 absorption limits the use of such a platform for wavelengths >4 μm. We have previously reported in Refs. [31,32] Ge-on-Si absorption modulators based on free-carrier injection through a lateral PIN junction at a waveguide of 3.8 μm under DC operation. In this work, we present detailed device design, fabrication, and characterization, and we extend this work to demonstrate refractive index modulation at 3.8 μm to investigate the RF performance of the devices and to demonstrate modulators operating at 8 μm.

2. DESIGN OF Ge-ON-Si CARRIER INJECTION MODULATORS

The modulators were based on the waveguides that were previously demonstrated in Refs. [15] and [20] for 3.8 μm and 8 μm, respectively. The devices were implemented on the Ge-on-Si substrate with a core thickness (T_{Rib}) of approximately 3 μm, a slab thickness (T_{Slab}) of 1.3 μm, and an etch depth of 1.7 μm. The core width (W_{Rib}) was designed to be 2.7 μm for $\lambda = 3.8$ μm and 3.2 μm for $\lambda = 8$ μm devices. The waveguides were designed for single-mode propagation. The cross section of the PIN diode is shown in the schematic in Fig. 1(a).

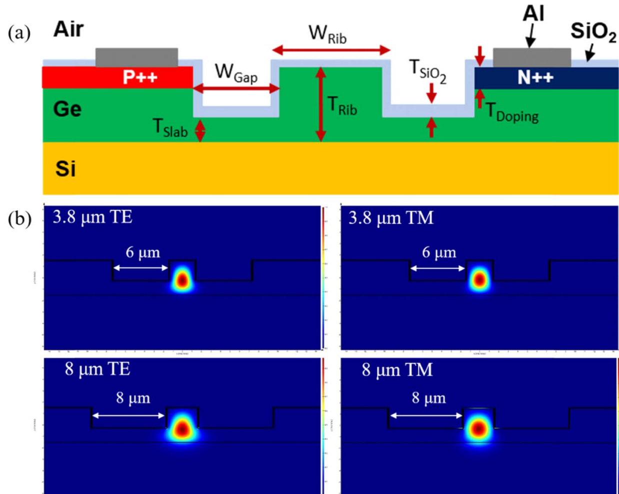

Fig. 1. (a) Schematic of the PIN junction modulator cross section. (b) The mode profiles for Ge-on-Si rib waveguides at 3.8 and 8 μm wavelengths, modeled using Lumerical Mode Solutions.

To avoid potential issues that might be caused by a nonuniform implant mask thickness resulting from the large rib waveguide etch depth, the doping implantation steps were conducted before waveguide etching. As a consequence, the contact doping had to be placed in the unetched Ge slab regions that were at least several micrometers away from the waveguide core as shown in Fig. 1(a). The target doping concentrations were 10^{19} cm^{-3} for both P++ and N++ doping. Since the etched region served as a lateral waveguide cladding, its width W_{Gap} had to be sufficiently large to suppress mode leakage towards the unetched side slabs. In addition, the 3-μm-thick Ge layer could not be doped through the whole thickness. This would require excessively high doping energy. The target doping depth (T_{Doping}) was set to be 500 nm. W_{Gap} was varied between 6 and 8 μm for devices operating at 3.8 μm, and it was set to be 8 μm for the 8-μm modulator operation. The simulated mode profiles are shown in Fig. 1(b), and the simulations showed that these values of W_{Gap} were sufficient to both prevent mode leakage and optical absorption in the highly doped regions.

All devices operating at 3.8 μm were designed with grating couplers to afford out-of-plane light coupling between optical fibers and on-chip Ge-on-Si waveguides. The grating couplers were similar to those previously published in Refs. [25,33], but they were re-designed for a 3-μm-thick Ge layer and 1.7-μm etching. The grating coupler was 26 μm wide with a grating period of 3.06 μm and duty cycle of 0.596. A 1-mm-long inverse taper excitation was used at the input to the grating coupler with a tip width of 1.1 μm. This injection waveguide arrangement minimized back-reflections into the waveguide as described in Ref. [33].

The devices for 8 μm were designed with end-fire light coupling into the waveguide via a linear edge taper. The end waveguide width was 20 μm at the edge facet, and a 1-mm-long taper was connected to the single-mode waveguide. At the output, a grating coupler was used to redirect light towards a long-wave infrared (LWIR) camera that was used for imaging. These grating couplers were the same as those described in

Ref. [20], with an etch depth of 1 μm, and they were designed for imaging by the camera.

Two kinds of modulators were designed for the 3.8-μm wavelength. (i) Electro-absorption modulators (EAMs), which consisted of PIN diodes integrated with 1-mm-long straight waveguides. The optical absorption change created by free-carrier injection into the waveguide directly creates an optical intensity change. (ii) Mach–Zehnder modulators (MZMs), in which a PIN diode is integrated with the waveguide in one arm of a Mach–Zehnder interferometer (MZI), and the change in refractive index introduced by free-carrier injection into the waveguide core creates a phase change, which is converted into an intensity modulation by the MZI. 1×2 multimode interference (MMI) couplers were used as the splitter and combiner in the MZI. The multimode region of the MMI was 14 μm wide and 106.5 μm long. The output ports had a center-to-center spacing of 7.25 μm, and the input and output ports were tapered from the single-mode waveguide width out to a maximum width of 6.75 μm over a 20-μm length. The MZIs were imbalanced with a 1-mm-long phase shifter and a 600-μm-long arm difference. Only the EAM devices were investigated at a wavelength of 8 μm, and they had a PIN diode length of 2 mm.

According to literature data, the SiO_2 top cladding is expected to be extremely lossy ($>10^4$ dB/cm [34]) at 8 μm; mode simulations indicate that it would introduce approximately 100 dB/cm to the waveguide propagation loss. In this fabrication run, we chose to accept this source of excess loss to simplify fabrication, but an alternative option would be to either use a different cladding material with lower absorption or to introduce another lithography step and etch away the SiO_2 directly above the waveguide.

3. FABRICATION PROCESSES

Chip fabrication was carried out at the Southampton Nanofabrication Centre, University of Southampton. The process flow for the Ge-on-Si modulator fabrication is shown in Fig. 2. Commercially purchased 6″ (150 mm) Ge-on-Si wafers with a 3-μm-thick Ge layer were used [Fig. 2(a)]. The $\lambda = 8$ μm gratings were defined using e-beam lithography, followed by inductively coupled plasma (ICP) etching. Alignment marks were also etched in this step for use in all subsequent steps [Fig. 2(b)]. 1.5-μm-thick SiO_2 was deposited on top by plasma-enhanced chemical vapor deposition (PECVD), serving as a hard mask for ion implantation [Fig. 2(c)]. The hard mask was patterned with optical lithography using S1813 photoresist followed by HF wet etching. The ion implantation was conducted at the Ion Beam Center, University of Surrey. Chain ion implantations of boron and subsequently phosphorous were conducted to realize both a high concentration at the surface for good Ohmic contact and doping depths (T_{Doping}) of 500 nm. For the boron doping, implant energies of 200, 100, 50, and 20 keV with corresponding dose levels of 5×10^{15}, 2.5×10^{15}, 1.5×10^{15}, and 1×10^{15} cm^{-2} were used. After ion implantation, the oxide hard mask was totally removed by HF wet etching. The same process was followed to carry out the phosphorus implant, with doping energies of 200, 70, and 20 keV and with the corresponding doses of 2.2×10^{15}, 6.3×10^{14}, and 1.9×10^{14} cm^{-2} [Fig. 2(d)]. At this stage, e-beam lithography and ICP etching were used to etch the waveguides and grating couplers for 3.8-μm operation [Fig. 2(e)]. A 100 nm SiO_2 layer (T_{SiO_2}) was deposited by PECVD, and vias were etched through the SiO_2 to allow contact with the doped regions. A passivation step was carried out, after which 100-nm-thick aluminum electrodes were deposited by e-beam evaporation and patterned using the lift-off technique at chip scale. Figure 3 shows an optical microscope image of the fabricated EAM working at 3.8 μm, and Fig. 4 shows a scanning electron microscope image of the top view of one of the PIN diodes.

4. CHARACTERIZATION AND ANALYSIS

A. Ohmic Contact Performance of 3.8-μm-Wavelength Devices

Circular transmission lines were fabricated on some chips in order to measure the contact and sheet resistances [35]. The resistivity was calculated to be 1.8×10^{-3} $\Omega \cdot$ cm for P++ doping and 1.0×10^{-3} $\Omega \cdot$ cm for N++ doping, respectively. According to Ref. [36], this corresponds to doping concentrations of 10^{19} cm^{-3} for both P++ and N++ doping. The contact resistivity was calculated to be 7.7×10^{-4} $\Omega \cdot \text{cm}^2$ for N-type and 1.8×10^{-4} $\Omega \cdot \text{cm}^2$ for P-type contact. The contact resistivity of the

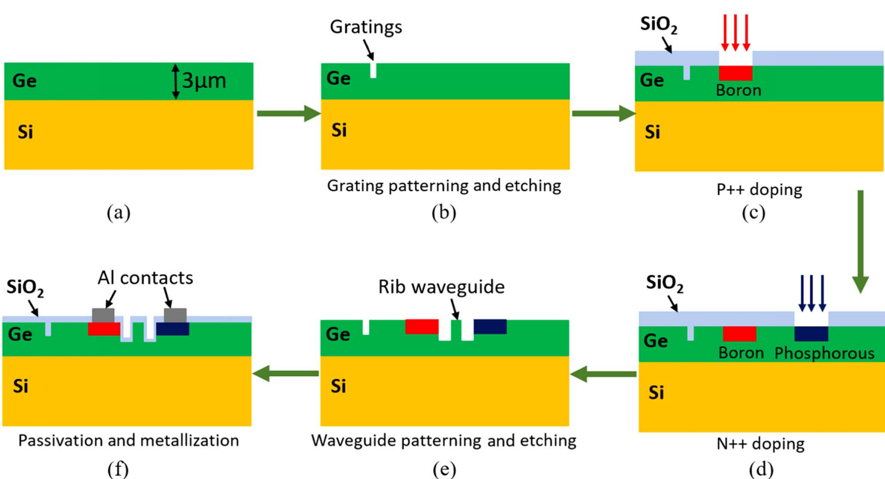

Fig. 2. Schematic illustration of the process flow used for the fabrication of Ge-on-Si waveguide modulators.

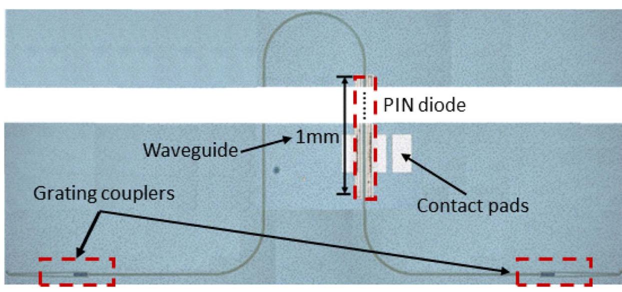

Fig. 3. Optical microscope images of the EAM devices at 3.8 μm. The image is composed of two images that have been stitched together, since the 1-mm PIN diode length does not fit in the microscope field of view. The horizontal white strip near the middle of the figure separates the two parts.

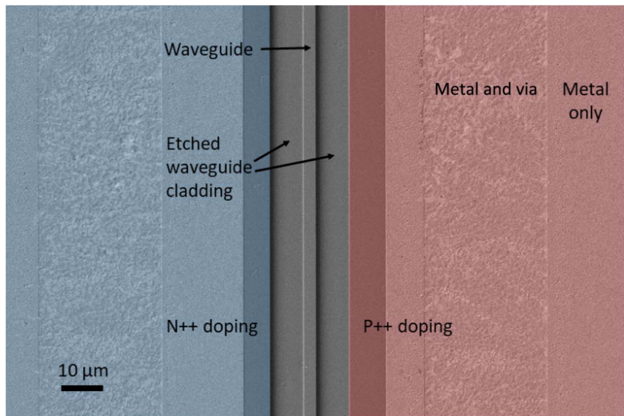

Fig. 4. Top view scanning electron microscope image of the PIN diode. The waveguide and etched lateral cladding are in the middle of the image in grey. The blue shaded region on the left is N++ doped, while the red region on the right is P++ doped. On both the P++- and N++-doped side regions, rough surfaces are visible, the areas in which vias through the SiO_2 top cladding have been etched for the formation of Ohmic contacts.

Ohmic contacts is much higher than the resistivity reported in literature, which was around $10^{-7}\ \Omega \cdot \mathrm{cm}^2$ [37]. The contact resistance of our device is calculated to be 2.57 Ω for N-type and 0.8 Ω for P-type contact. The high contact resistance would cause a large part of the forward bias voltage applied across a PIN diode to be dropped across the contacts. This way, the required driving voltage would be much higher than expected. The reverse bias leakage current measured across the PIN diodes was negligible (i.e., $<10^{-4}$ A under −4 V bias voltage in a 0.25-mm-long diode) compared to the same forward bias current. This shows that there is very little surface leakage current when a forward bias is applied across the PIN diodes.

B. Electro-Absorption and Electro-Refraction Modulators for 3.8 μm

The experimental setup for 3.8-μm device operation is shown in Fig. 5. Optical characterization was carried out using an MIR experimental setup that consists of a tunable quantum cascade laser (QCL) with a center wavelength of 3.8 μm and a custom

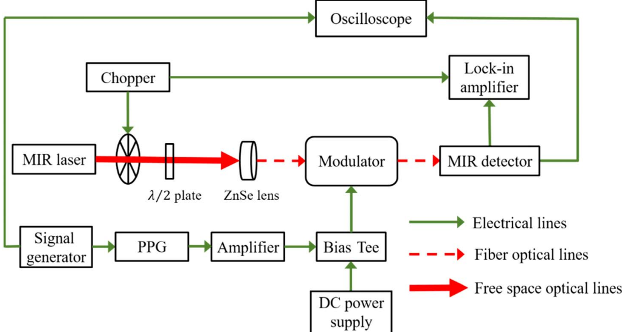

Fig. 5. Schematic diagram of the experimental setup for modulator characterization (PPG, pulse pattern generator).

built HgCdTe photodetector (Vigo Systems PVI-4TE-4) with a −3-dB high cutoff frequency larger than 400 MHz. The HgCdTe detector is AC coupled. This results in the DC component of any optical signal being filtered from its electrical output. The light polarization is adjusted for TE polarization (to suit the grating couplers) using a half-wave plate that is placed at the linearly polarized laser output. The light is then coupled into MIR fibers using a ZnSe lens. Single-mode ZrF_4 MIR fibers with 9-μm core and 125-μm cladding diameters are used to couple light to and from the chip.

For the DC measurements, a combination of a chopper in the optical beam operating at ∼250 Hz and a lock-in amplifier connected to the detector output is used to improve the SNR and to add a periodic component to the optical beam so that it could be measured by the detector. For the RF measurement, a signal generator and pulse pattern generator (PPG) are employed to generate a $2^7 - 1$ pseudo-random binary sequence (PRBS). The signal is then amplified using a microwave amplifier. Since the PIN junction operates in the carrier injection regime, a bias-tee is used to combine the RF signal and the DC bias. The output optical signal is directly detected by the HgCdTe detector and then sampled by a real-time storage oscilloscope. The eye diagram is then constructed in MATLAB from the recorded long bit sequence.

When testing the passive optical performance of the devices, we observed a high degree of variation in the absolute values of the transmission through nominally identical normalization structures (e.g., straight waveguides). This limited reliable measurements of modulator insertion losses and waveguide propagation losses. The cause of this is unclear, but it may be related to a sensitivity of the grating couplers to fabrication variations, or it may be related to other fabrication defects.

The DC performance of the EAM with W_{Gap} of 6 μm operating at 3.8 μm wavelength is first investigated. Figure 6(a) shows the normalized transmission of the device over the 3720–3820 nm wavelength range under different DC bias voltages. The measured wavelength range was limited by the laser transmission range as well as by the grating coupler bandwidth. However, the modulator is intrinsically limited only by the waveguide bandwidth, since free-carrier absorption in Ge is very strong throughout the MIR [30]. Figure 6(b) shows the modulation depth of the device under DC voltages from 0 to 7 V as measured at a wavelength of 3765 nm. The

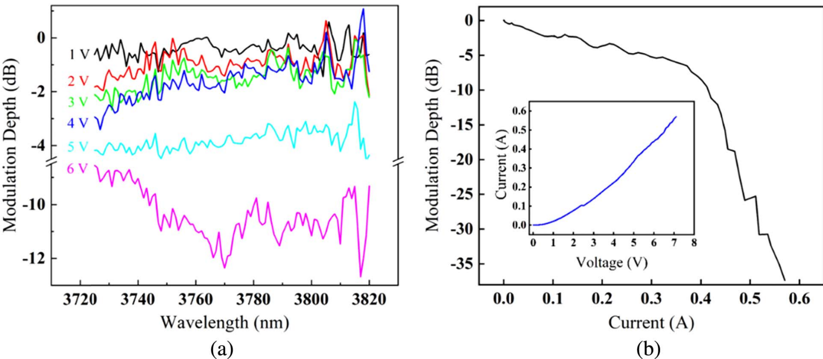

Fig. 6. (a) Modulation depth as a function of the wavelength under different bias conditions. (b) Modulation depth as a function of current at a wavelength of 3765 nm. Inset: current-voltage device characteristic.

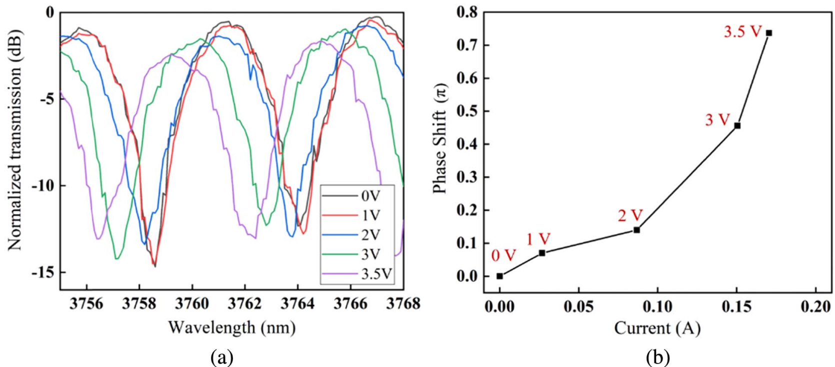

Fig. 7. (a) Optical spectra of the MZM under several DC voltages. The spectral transmission is normalized to the highest transmission as seen through the device (so that the offset of transmission from zero does not represent the insertion loss). (b) Phase shift versus current of the MZM.

modulation depth reaches 35 dB under 7 V bias with a corresponding current flow of 0.56 A. The measured current-voltage (*I-V*) curve of this device is shown in the inset of Fig. 6(b).

Next we studied the DC performance of the fabricated MZM devices. The optical spectrum of the MZM with W_{Gap} of 6 μm under different DC forward bias voltages is shown in Fig. 7(a). The DC extinction ratio is greater than 13 dB for a maximum achieved phase shift of 0.75π under a voltage of 3.5 V as shown in Fig. 7(b). The wavelength-dependent extinction ratio is decreased under higher bias voltage, which is caused by the free-carrier loss. The design of an unbalanced MZI could be used to compensate for the free-carrier loss. The corresponding $V_{\pi} \cdot L$ is 0.47 V · cm. We verified that the direction of the wavelength shift of the MZM transmission spectra with a bias applied is consistent with a negative refractive index change as would be expected from a change in the free-carrier concentration. There is likely to be some heating in this device that would cause a positive change in the refractive index of the waveguide and would thus reduce the efficiency of the phase shifter.

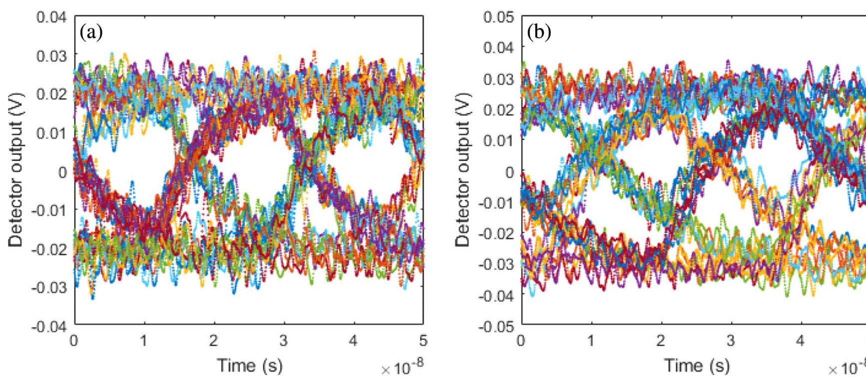

Fig. 8. Eye diagrams measured at 60 MHz for (a) EAM and (b) MZM.

The RF performance of the EAM devices was investigated at 3.8 μm. The 60-MHz eye diagrams generated by the EAM and MZM are shown in Figs. 8(a) and 8(b), respectively. The driving voltage for both was $2.5V_{pp}$ with a 1.9-V DC bias. Because the detector does not measure the DC component of the optical signal, it is impossible to reliably measure the extinction ratio from the eye diagram. Nevertheless, it is clear that both devices still exhibit open eye diagrams at 60 MHz.

C. Electro-Absorption Modulator Operating at 8 μm

The 8-μm device was measured using the setup described in detail in Ref. [20]. Light from a Pranalytica tunable QCL is coupled into an As_2Se_3 fiber using a ZnSe objective lens. The fiber leads to the waveguide edge facet. DC probes are used to apply a DC voltage across the PIN diode. An FLIR SC660 camera images the surface of the chip, and the grating at the waveguide output radiates light up towards the camera. The reasons for using this coupling scheme instead of other more conventional coupling schemes are discussed in Ref. [20].

To measure the light transmission through a grating coupler as observed by the camera, at each applied DC voltage a video is recorded that contains frames with both the laser switched on and the laser switched off. The background is corrected by subtracting one of the "laser off" frames from one of the "laser on" frames [Fig. 9(a)] so that only laser light is visible in the resulting image as shown in Fig. 9(b). The pixel intensities in an area around the grating coupler are summed together to give a value that is proportional to the total grating coupler transmission.

Figure 10(a) shows the resulting plot of modulation depth as a function of the varying DC forward-bias voltages. As shown in Fig. 10(a), the maximum achieved modulation depth is 2.5 dB under 7 V voltage. The contact resistances of the EAM devices at 3.8 and 8 μm are different due to variation of the contact resistance among the different chips. As shown in the inset of Fig. 10(a), under the same voltage, the current per unit length of the long wavelength devices is much lower, which means worse contacts. Therefore, the modulation depth versus voltage curves cannot be compared directly, but instead the current versus modulation depth curves have been plotted in Fig. 10(b) for two devices with the same separation ($W_{\mathrm{Gap}} = 8$ μm) between the waveguide edge and the Ohmic contacts. Since the PIN diodes are of different lengths, the x axis is plotted as diode current per unit diode length, and the y axis is the absorption introduced by the carrier injection in decibels per centimeter (dB/cm). The only other difference between the two devices is the wider single-mode waveguide width at the longer wavelength (i.e., 3.2 μm at $\lambda = 8$ μm compared to 2.7 μm at $\lambda = 3.8$ μm).

As a first-order approximation, we fit a linear curve to both sets of current versus modulation depth data, and we find that at 3.8 μm wavelength the fitted line has a slope of 3.43 dB/A, while at 8 μm wavelength there is a 16.8 dB/A slope. Since in two PIN diodes with the same dimensions and the same injection current the charge carrier concentration would be expected to be approximately the same, we can use this fitted slope as a proxy for comparing the absorption coefficient versus carrier concentration relationships at the two wavelengths and estimate that free-carrier absorption is approximately 4.9 times greater at 8 μm than at 3.8 μm. Of course, since the longer-wavelength waveguide is 0.5 μm wider, the injection volume is ∼5% larger, and therefore the charge carrier concentration at $\lambda = 8$ μm is likely slightly lower, and we can expect that we slightly underestimate the relative difference in absorption at the two wavelengths.

If we use the theoretical equations for $\Delta\alpha$ from Ref. [30] for a charge carrier concentration of $\Delta N_e = \Delta N_h$ in the range of 10^{16} to 10^{18} cm^{-3}, we would expect that $\Delta\alpha$ is 4.7 to 4.9 times greater at $\lambda = 8$ μm than at 3.8 μm, which agrees well with the experimentally measured difference.

5. DISCUSSION

The total power consumption for the 1-mm-long MZM device at $\lambda = 3.8$ μm is calculated to be 595 mW (3.5 V × 0.17 A) for 0.75π phase shift. Most of the power is consumed in the contact region and the undoped slab region. The measured devices exhibited significantly lower modulation efficiencies and higher power consumption than is routinely expected in NIR silicon photonic carrier injection modulators, despite the expectation of a very strong free-carrier effect in Ge. There are several likely causes of this. (i) The large spacing between the P-type and N-type contacts in the PIN diodes used in this demonstration requires the carriers to be injected into a large region, and therefore the overlap between the injected carriers and the waveguide mode is low. (ii) The Ohmic contacts exhibit high resistance and thus reduce the injected carrier concentration for a given applied voltage. (iii) A relatively high defect concentration in Ge at the Ge–Si interface, as a result of a

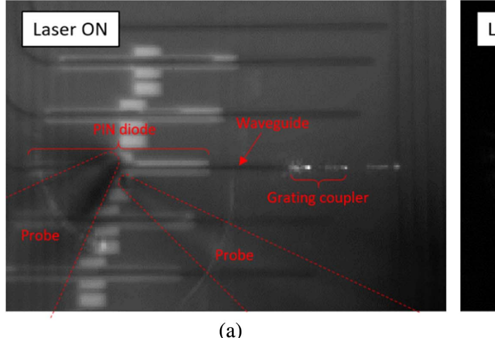

(a)

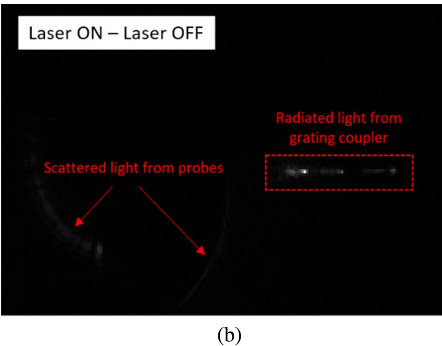

(b)

Fig. 9. Captured LWIR camera image with the QCL tuned to $\lambda = 8$ μm: (a) when the laser is emitting, (b) when the "laser off" frame is subtracted from the "laser on" frame. White areas show high infrared light intensity, and dark areas show low intensity.

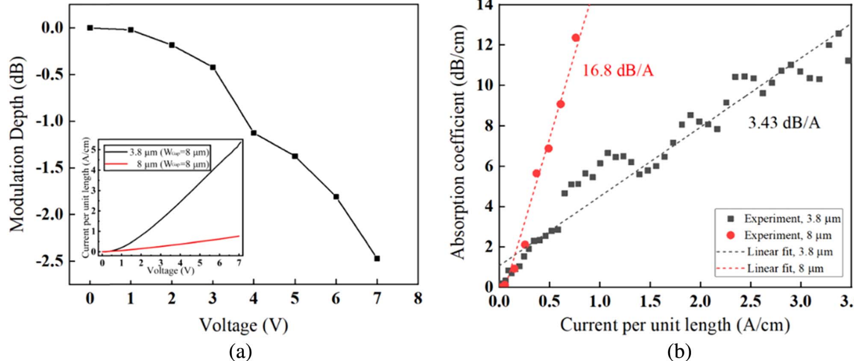

Fig. 10. (a) Extinction ratio as a function of the applied voltage for a 2-mm-long EAM operating at a wavelength of 8 μm. Inset: current per unit length versus voltage curves at a wavelength of 8 μm (2-mm-long diode) and of 3.8 μm (1-mm-long diode) for EAM devices with the same 8-μm contact separation (W_{Gap}). (b) Absorption coefficient versus current per unit PIN diode length at a wavelength of 8 μm (2-mm-long diode) and of 3.8 μm (1-mm-long diode) for EAM devices with the same contact separation (W_{Gap}).

Si and Ge lattice constants mismatch, reduces the carrier lifetime; coupled with the long distance over which carriers are injected, this would substantially reduce the carrier concentration in the waveguide core. The device's efficiency could be significantly improved by using a more optimized Ohmic contact fabrication process and by placing the Ohmic contacts much closer to the waveguide. In this work, the decision to use a large contact separation stemmed only from the choice of a very conservative fabrication process. Introducing additional lower-concentration P- and N-type implantation steps in the slab region adjacent to the waveguide would also reduce the diode resistance and injection volume without introducing too much excess optical absorption.

It is worth noting that it is challenging to use these experimental measurements to directly verify the theoretical predictions of the strength of the free-carrier effect in Ge presented in Ref. [30] since the actual carrier concentration in the waveguides is unknown and cannot be readily measured.

If we compare the EAM and MZM devices for 3.8 μm, which have nominally the same PIN diode sections, we can try to estimate the absorption introduced in the phase shifter when applying a π phase shift. Based on Fig. 7(b), for a π phase shift (in a situation where the devices were to be driven by 3.5 V but a 1.33-mm-long PIN diode was used), a 0.23-A injection current would be required. If we assume that the same injection current results in the same charge carrier concentration in both devices, from Fig. 6(b) we can say that a 0.23-A injection current produces 3.85 dB of absorption in the EAM device. For many phase shifter applications (such as beam steering) this level of excess loss will be unacceptable, and the problem will become even more severe at longer wavelengths where the free-carrier absorption is stronger. In a conventional 1×2 MZI switch, high excess free-carrier loss will increase the insertion loss and crosstalk of the switch. Soref *et al.* have proposed alternative Ge-waveguide-based switch designs that use the free-carrier absorption and refraction effects that would be expected to circumvent much of the parasitic effect of free-carrier absorption on insertion loss and crosstalk [38,39].

6. CONCLUSIONS

In this work, MIR electro-optic modulators based on the Ge-on-Si platform have been investigated at wavelengths up to 8 μm. A fabricated 1-mm-long EAM exhibited a DC modulation depth in excess of 35 dB at 3.8 μm wavelength, and an MZM with a 1-mm-long phase shifter at the same wavelength had a modulation depth of 13 dB with a $V_\pi \cdot L$ of 0.47 V · cm. When driven by an RF signal, 60-MHz OOK modulation was demonstrated in both the EAM and MZM devices. An EAM device has also been demonstrated at a wavelength of 8 μm with a 2.5-dB modulation depth for a 7-V DC forward bias in a 2-mm-long PIN diode. The measurements indicate that the injected free-carrier absorption is more than 4.9 times greater at 8 μm than at 3.8 μm for the same carrier concentration, which is consistent with the theoretical predictions of Ref. [30]. The modulation efficiency of all of these modulators would be expected to increase significantly with optimization of the Ohmic contact separation and with improved Ohmic contact fabrication.

The devices that have been characterized represent the first demonstrations of free-carrier injection-based modulators in the Ge-on-Si material platform to our knowledge, and the modulation at 8 μm wavelength represents the longest wavelength at which modulation in a group-IV waveguide has been demonstrated to date. These results also show that PIN-diode-based carrier injection modulators can be extremely broadband since the devices demonstrated here, which are identical in all aspects except the waveguide width, have been used at wavelengths that are separated by more than an octave in frequency.

Funding. Engineering and Physical Sciences Research Council (EPSRC) (EP/N00762X/1, EP/N013247/1, EP/R004951/1); Royal Academy of Engineering (RF201617/16/33); National Research Foundation Singapore (NRF) (NRF-CRP12-2013-04); Royal Society (UF150325); European Project Cosmicc (H2020-ICT-27-2015-688516); China Scholarship Council (CSC); State Key Laboratory of Advanced Optical Communication Systems and Networks,

China; European Research Council under the European Union's Seventh Framework Programme (FP7/2007-2013); H2020 European Research Council (ERC) (291216).

Acknowledgment. The authors are grateful to R. Gwilliam, A. Z. Khokhar, S. A. Reynolds, S. Stanković, M. Banakar, K. Grabska, J. S. Wilkinson, and G. T. Reed for assistance in fabrication and measurement processes and for useful discussion. T. Li acknowledges support from the China Scholarship Council and State Key Laboratory of Advanced Optical Communication Systems and Networks, China. All data supporting this study are openly available at https://doi.org/10.5258/SOTON/D0946.

REFERENCES

1. G. T. Reed, G. Mashanovich, F. Y. Gardes, and D. J. Thomson, "Silicon optical modulators," Nat. Photonics **4**, 518–526 (2010).
2. Z. Zhou, R. Chen, X. Li, and T. Li, "Development trends in silicon photonics for data centers," Opt. Fiber Technol. **44**, 13–23 (2018).
3. P. Dong, Y.-K. Chen, G.-H. Duan, and D. T. Neilson, "Silicon photonic devices and integrated circuits," Nanophotonics **3**, 215–228 (2014).
4. T. Li, J. Zhang, H. Yi, W. Tan, Q. Long, Z. Zhou, X. Wang, and H. Wu, "Low-voltage, high speed, compact silicon modulator for BPSK modulation," Opt. Express **21**, 23410–23415 (2013).
5. T. Li, D. Wang, J. Zhang, Z. Zhou, F. Zhang, X. Wang, and H. Wu, "Demonstration of 6.25 Gbaud advanced modulation formats with subcarrier multiplexed technique on silicon Mach-Zehnder modulator," Opt. Express **22**, 19818–19823 (2014).
6. W. Cao, D. Hagan, D. J. Thomson, M. Nedeljkovic, C. G. Littlejohns, A. Knights, S. Alam, J. Wang, F. Gardes, W. Zhang, S. Liu, K. Li, M. S. Rouifed, G. Xin, W. Wang, H. Wang, G. T. Reed, and G. Z. Mashanovich, "High-speed silicon modulators for the 2 μm wavelength band," Optica **5**, 1055–1062 (2018).
7. Y. Zou, S. Chakravarty, C.-J. Chung, X. Xu, and R. T. Chen, "Mid-infrared silicon photonic waveguides and devices," Photon. Res. **6**, 254–276 (2018).
8. R. A. Soref, S. J. Emelett, and W. R. Buchwald, "Silicon waveguided components for the long-wave infrared region," J. Opt. A **8**, 840–848 (2006).
9. T. Baehr-Jones, A. Spott, R. Ilic, A. Spott, B. Penkov, W. Asher, and M. Hochberg, "Silicon-on-sapphire integrated waveguides for the mid-infrared," Opt. Express **18**, 12127–12135 (2010).
10. S. Khan, J. Chiles, J. Ma, and S. Fathpour, "Silicon-on-nitride waveguides for mid-and near-infrared integrated photonics," Appl. Phys. Lett. **102**, 121104 (2013).
11. J. Kang, M. Takenaka, and S. Takagi, "Novel Ge waveguide platform on Ge-on-insulator wafer for mid-infrared photonic integrated circuits," Opt. Express **24**, 11855–11864 (2016).
12. V. Vakarin, J. M. Ramírez, J. Frigerio, A. Ballabio, X. Le Roux, Q. Liu, D. Bouville, L. Vivien, G. Isella, and D. Marris-Morini, "Ultra-wideband Ge-rich silicon germanium integrated Mach-Zehnder interferometer for mid-infrared spectroscopy," Opt. Lett. **42**, 3482–3485 (2017).
13. J.-M. Ramirez, Q. Liu, V. Vakarin, J. Frigerio, A. Ballabio, X. Le Roux, D. Bouville, L. Vivien, G. Isella, and D. Marris-Morini, "Graded SiGe waveguides with broadband low-loss propagation in the mid infrared," Opt. Express **26**, 870–877 (2018).
14. M. Sinobad, C. Monat, B. Luther-Davies, P. Ma, S. Madden, D. J. Moss, A. Mitchell, D. Allioux, R. Orobtchouk, S. Boutami, J.-M. Hartmann, J.-M. Fedeli, and C. Grillet, "Mid-infrared octave spanning supercontinuum generation to 8.5 μm in silicon-germanium waveguides," Optica **5**, 360–366 (2018).
15. M. Nedeljkovic, J. Soler Penades, C. J. Mitchell, T. Dominquez Bucio, A. Z. Khokhar, C. Littlejohns, F. Y. Gardes, and G. Z. Mashanovich, "Surface grating coupled low loss Ge-on-Si rib waveguides and multi-mode interferometers," IEEE Photon. Technol. Lett. **27**, 1040–1043 (2015).
16. Y. C. Chang, V. Paeder, L. Hvozdara, J. M. Hartmann, and H. P. Herzig, "Low-loss germanium strip waveguides on silicon for the mid-infrared," Opt. Lett. **37**, 2883–2885 (2012).
17. W. Li, P. Anantha, S. Bao, K. H. Lee, X. Guo, T. Hu, L. Zhang, H. Wang, R. Soref, and C. S. Tan, "Germanium-on-silicon nitride waveguides for mid-infrared integrated photonics," Appl. Phys. Lett. **109**, 241101 (2016).
18. N. Hô, M. C. Phillips, H. Qiao, P. J. Allen, K. Krishnaswami, B. J. Riley, T. L. Myers, and N. C. Anheier, Jr., "Single-mode low-loss chalcogenide glass waveguides for the mid-infrared," Opt. Lett. **31**, 1860–1862 (2006).
19. R. Soref, "Mid-infrared photonics in silicon and germanium," Nat. Photonics **4**, 495–497 (2010).
20. M. Nedeljkovic, J. S. Penades, V. Mittal, G. S. Murugan, A. Z. Khokhar, C. LittleJohns, L. G. Carpenter, C. B. E. Gawith, J. S. Wilkinson, and G. Mashanovich, "Germanium-on-silicon waveguides operating at mid-infrared wavelengths up to 8.5 μm," Opt. Express **25**, 27431–27441 (2017).
21. D. A. Kozak, T. H. Stievater, R. Mahon, and W. S. Rabinovich, "Germanium-on-silicon waveguides at wavelengths from 6.85 to 11.25 microns," IEEE J. Sel. Top. Quantum Electron. **24**, 8200804 (2018).
22. K. Gallacher, R. W. Millar, U. Griškevičiūte, L. Baldassarre, M. Sorel, M. Ortolani, and D. J. Paul, "Low loss Ge-on-Si waveguides operating in the 8-14 μm atmospheric transmission window," Opt. Express **26**, 25667–25675 (2018).
23. A. Malik, M. Muneeb, Y. Shimura, J. Van Campenhout, R. Loo, and G. Roelkens, "Germanium-on-silicon planar concave grating wavelength (de)multiplexers in the mid-infrared," Appl. Phys. Lett. **103**, 161119 (2013).
24. A. Malik, M. Muneeb, S. Pathak, Y. Shimura, J. Van Campenhout, R. Loo, and G. Roelkens, "Germanium-on-silicon mid-infrared arrayed waveguide grating multiplexers," IEEE Photon. Technol. Lett. **25**, 1805–1808 (2013).
25. C. Alonso-Ramos, M. Nedeljkovic, D. Benedikovic, J. S. Penades, C. G. Littlejohns, A. Z. Khokhar, D. Perez-Galacho, L. Vivien, P. Cheben, and G. Z. Mashanovich, "Germanium-on-silicon mid-infrared grating couplers with low-reflectivity inverse taper excitation," Opt. Lett. **41**, 4324–4327 (2016).
26. A. Malik, S. Dwivedi, L. Van Landschoot, M. Muneeb, Y. Shimura, G. Lepage, J. Van Campenhout, W. Vanherle, T. Van Opstal, R. Loo, and G. Roelkens, "Ge-on-Si and Ge-on-SOI thermo-optic phase shifters for the mid-infrared," Opt. Express **22**, 28479–28488 (2014).
27. M. Nedeljkovic, S. Stankovic, C. J. Mitchell, A. Z. Khokhar, S. A. Reynolds, D. J. Thomson, F. Y. Gardes, C. G. Littlejohns, G. T. Reed, and G. Z. Mashanovich, "Mid-infrared thermo-optic modulators in SOI," IEEE Photon. Technol. Lett. **26**, 1352–1355 (2014).
28. G. Z. Mashanovich, M. M. Milošević, M. Nedeljkovic, N. Owens, B. Xiong, E. J. Teo, and Y. Hu, "Low loss silicon waveguides for the mid-infrared," Opt. Express **19**, 7112–7119 (2011).
29. J. Kang, Z. Cheng, W. Zhou, T. H. Xiao, K. L. Gopalakrisna, M. Takenaka, H. K. Tsang, and K. Goda, "Focusing subwavelength grating coupler for mid-infrared suspended membrane germanium waveguides," Opt. Lett. **42**, 2094–2097 (2017).
30. M. Nedeljkovic, R. Soref, and G. Z. Mashanovich, "Predictions of free-carrier electroabsorption and electrorefraction in germanium," IEEE Photon. J. **7**, 2600214 (2015).
31. G. Z. Mashanovich, M. Nedeljkovic, J. Soler-Penades, Z. Qu, W. Cao, A. Osmon, Y. Wu, C. J. Stirling, Y. Qi, Y. Xu-Cheng, L. Reid, C. G. Littlejohns, J. Kang, Z. Zhao, M. Takenaka, T. Li, Z. Zhou, F. Y. Gardes, D. J. Thomson, and G. T. Reed, "Group IV mid-infrared photonics [Invited]," Opt. Mater. Express **8**, 2276–2286 (2018).
32. T. Li, M. Nedeljkovic, N. Hattasan, A. Z. Khokhar, S. A. Reynolds, S. Stankovic, M. Banakar, W. Cao, Z. Qu, C. G. Littlejohns, J. S. Penades, K. Grabska, L. Mastronardi, D. J. Thomson, F. Y. Gardes, G. T. Reed, H. Wu, Z. Zhou, and G. Z. Mashanovich, "Mid-infrared Ge-on-Si electro-absorption modulator," in *IEEE 14th International Conference on Group IV Photonics (GFP)* (IEEE, 2017), pp. 7–8.
33. B. Troia, J. S. Penades, A. Z. Khokhar, M. Nedeljkovic, C. Alonso-Ramos, V. M. N. Passaro, and G. Z. Mashanovich, "Germanium-on-silicon Vernier-effect photonic microcavities for the mid-infrared," Opt. Lett. **41**, 610–613 (2016).

34. R. Kitamura, L. Pilon, and M. Jonasz, “Optical constants of silica glass from extreme ultraviolet to far infrared at near room temperature,” Appl. Opt. **46**, 8118–8133 (2007).
35. G. S. Marlow and M. B. Das, “The effects of contact size and non-zero metal resistance on the determination of specific contact resistance,” Solid-State Electron. **25**, 91–94 (1982).
36. M. Balkanski and R. F. Wallis, *Semiconductor Physics and Applications* (Oxford University, 2000).
37. K. Gallacher, P. Velha, D. J. Paul, I. MacLaren, M. Myronov, and D. R. Leadley, “Ohmic contacts to n-type germanium with low specific contact resistivity,” Appl. Phys. Lett. **100**, 022113 (2012).
38. R. Soref, J. R. Hendrickson, and J. Sweet, “Simulation of germanium nanobeam electro-optical 2×2 switches and 1×1 modulators for the 2 to 5 μm infrared region,” Opt. Express **24**, 9369–9382 (2016).
39. R. A. Soref, “Mid-infrared 2×2 electro-optical switching by silicon and germanium three-waveguide and four-waveguide directional couplers using free-carrier injection,” Photon. Res. **2**, 102–110 (2014).